Pergamon

PII: S0191–8141(98)00011–X

Journal of Structural Geology, Vol. 20, No. 6, pp. 681 to 694, 1998

0191-8141/98 $19.00 + 0.00

The origin of shape preferred orientations in mylonite: inferences from *in-situ* experiments on polycrystalline norcamphor

M. HERWEGH

Geologisches Institut, Universität Bern, Baltzerstr. 1, 3012 Bern, Switzerland
(herwegh@geo.unibe.ch)

and

M. R. HANDY

Institut für Geowissenschaften, Justus-Liebig Universität, Giessen, Germany

(*Received* 11 *February* 1997; *accepted in revised form* 23 *December* 1997)

Abstract—Polycrystalline norcamphor ($C_7H_{10}O$) undergoing plane strain simple shear in a see-through deformation rig develops intergranular microshears whose activity and orientation is closely related to shape preferred orientation (SPO) of dynamically recrystallized grains and grain aggregates. Intergranular microshears nucleate at 80–90° to the sample's shear zone boundary (SZB) and rotate synthetically toward this boundary. They accommodate increasing amounts of incremental shear strain at angles ranging from 40° to 60° (S_b orientation) with respect to the SZB. With progressive simple shear, both the rotation rate and the amount of strain accommodated by these microshears decrease, but strain accommodation increases as the microshears attain a lower angle (10–30°, S_a orientation) to the SZB. The microshears gradually deactivate as they acquire inclination angles to the SZB of less than 10°. The deactivation of such microshears is accompanied by the nucleation of fresh, high angle microshears. This heterogeneous deformation is associated with two shape preferred orientations in the norcamphor mylonite: A steep, oblique grain SPO comprising the long axes of dynamically recrystallized grains (40–60°) subparallel to the S_b-oriented microshears and gently inclined domainal SPO (20°) subparallel to the S_a-oriented microshears. The domain SPO is defined by the length axes of grain aggregates with a uniform crystallographic preferred orientation. The angle between domainal and grain SPOs is a potential measure of the bulk vorticity during mylonitization. © 1998 Elsevier Science Ltd. All rights reserved

INTRODUCTION

The preferred orientation of the shapes and boundaries of elongate grains and grain aggregates, often referred to as shape preferred orientation (or SPO), is a widely observed phenomenon in natural and experimental mylonites (e.g. quartz: Brunel, 1980; Knipe and Law, 1987; Dell'Angelo and Tullis, 1989; calcite: Schmid *et al*., 1987; olivine: Zhang and Karato, 1995; ice: Burg *et al*., 1986). In particular, the tendency in such rocks for SPOs to form at oblique angles to the mylonitic shear zone boundary (or SZB) allows one to deduce the sense of shear (e.g. Simpson and Schmid, 1983; Lister and Snoke, 1984) and is therefore of great practical use to field geologists in reconstructing the kinematic history of deformed rocks. Yet, an understanding of how SPOs form lags far behind its widespread application as an empirically reliable kinematic indicator.

Several mechanisms have been proposed for the origin and evolution of oblique SPOs in mylonitic rock. Simpson and Schmid (1983) believed that an oblique grain SPO forms as a result of dynamic recrystallization during the late stages of progressive noncoaxial shear, and therefore only reflects the kinematics of the latter stages of deformation. In contrast, Lister and Snoke (1984) proposed that grain SPO forms early during noncoaxial shear and is present throughout subsequent deformation. They argued that as dynamically recrystallized grains become elongate during deformation, their long axes rotate continuously toward parallelism with the shear zone boundary (SZB) until a sufficient amount of strain has accrued for the formation of new dynamically recrystallized grains. Grain-boundary migration recrystallization was therefore inferred to be an important renewal process that resets grain shape and so preserves oblique SPOs to high shear strains. Lister and Snoke (1984) aptly referred to this process as "resetting the finite strain clock". The importance of grain boundary migration in preserving SPO at elevated temperatures was confirmed in Ree's (1991) *in-situ* experiments on octachloropropane. Ree was able to generate a stable SPO at shear strains greater than 1.1. Simple shear of polycrystalline calcite (Schmid *et al*., 1987) and SEM electron channelling investigations on natural quartz mylonite (Lloyd *et al*., 1992) revealed that a combination of intra- and intercrystalline gliding may contribute to the formation of an oblique SPO. Karato and Masuda (1989) showed that stress-induced aniso-

tropic grain growth can also lead to the formation of an SPO in coaxially deformed quartz aggregates. *In-situ* experiments on polycrystalline norcamphor (Herwegh and Handy, 1996), an organic analogue for quartzite, revealed that the formation of an oblique grain SPO is closely related to localized, intergranular deformation. Unfortunately, this intergranular deformation could only be quantified to shear strains of 4, preventing us from drawing any conclusions about the strain distribution and SPO stability at the high shear strains ($\gamma > 8$) necessary to attain a steady state microstructure. Recently, Pauli *et al.*, (1996) presented a three-dimensional kinematic model in which intra- and intercrystalline glide lead to the formation of oblique

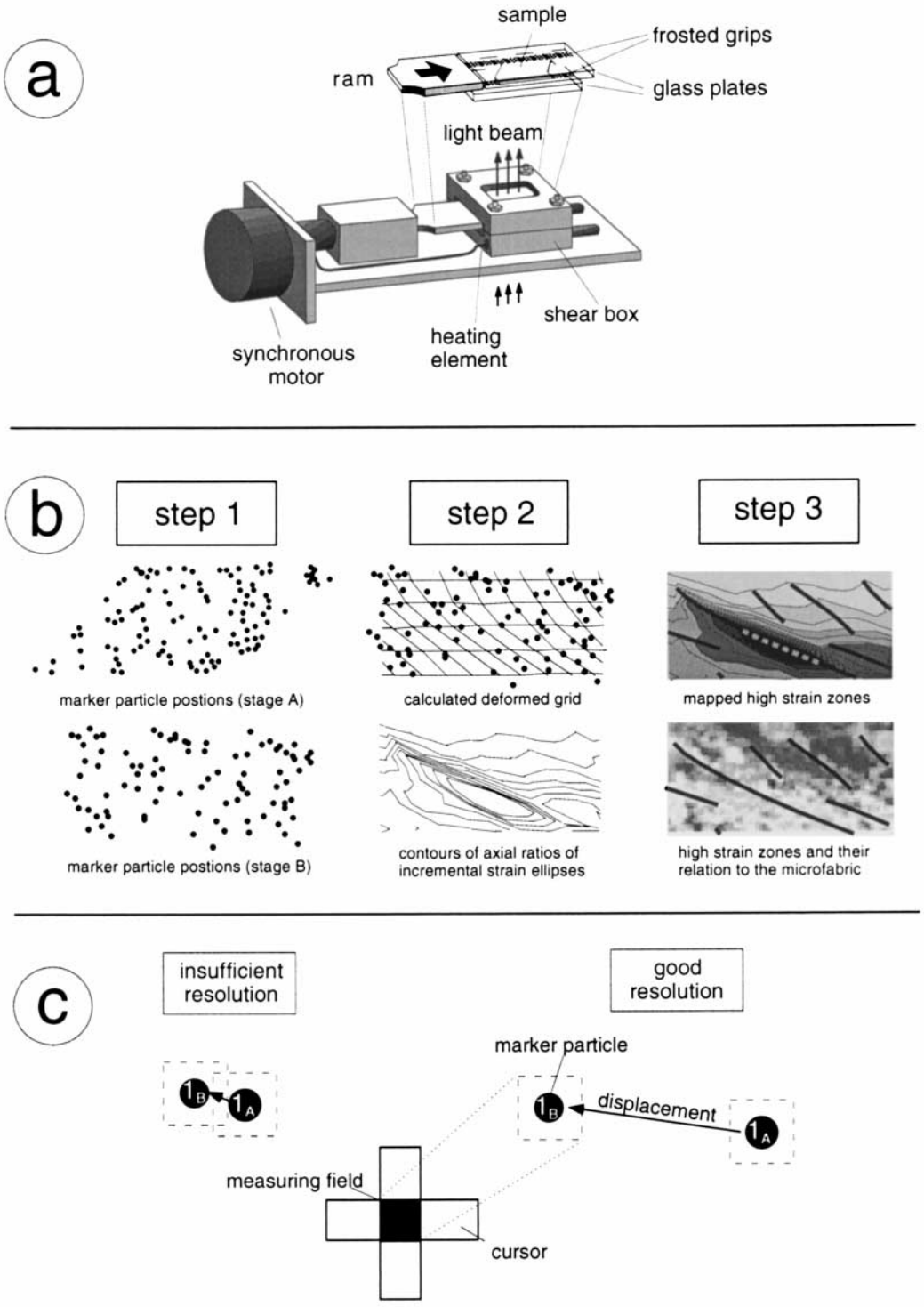

Fig. 1. Experimental setup and strain analysis: (a) Means–Urai deformation rig with sample undergoing simple shear between two thin sections, (b) three steps of strain analysis, (c) analytical error associated with a digitizing corundum marker particle (see text for explanation).

SPOs in quartz aggregates. As Lister and Snoke (1984) did before, Pauli *et al*. (1996) propose grain boundary migration recrystallization as the principal grain-shape resetting process involved in the preservation of oblique SPOs to high shear strains. Clearly, an understanding of how and when SPOs form is essential if they are to be used as reliable indicators of rocks' kinematic history. In assessing the work above, it is important to realize that, except for the work of Ree (1991) and Herwegh and Handy (1996), all previous studies were performed on natural and experimental samples in which only a single stage of a long deformational history is frozen in the microfabric.

It was with this limitation in mind that we conducted a series of high-strain experiments on polycrystalline norcamphor designed to examine the evolution of SPO, crystallographic preferred orientation (CPO), and small-scale localization phenomena directly under the optical microscope. After a description of the experimental and analytical procedures in the next section, we outline the evolution of microfabric heterogeneities in the norcamphor samples and characterize the strain localized history leading to steady state. In particular, we show that the development of steady state, grain and grain-aggregate SPOs is intimately linked to both intra- and intergranular microshearing, as well as to the conditions of deformation. The experimental results are then discussed in the context of existing models of microfabric evolution. Finally, a new model of SPO formation is proposed which explains several microfabric elements commonly observed in mylonitic rock.

EXPERIMENTAL PROCEDURE AND ANALYTICAL TECHNIQUES

Norcamphor ($C_7H_{10}O$) was deformed in plane strain, simple shear in a Means–Urai see-through apparatus (cf. Fig. 1a; Urai, 1987; Means, 1989) at four different strain rate and temperature conditions; (1) high temperature–low strain rate (HT–LS), (2) high temperature–high strain rate (HT–HS), (3) intermediate temperature–high strain rate (IT–HS) and (4) low temperature–high strain rate (LT–HS). The experimental conditions are listed in Table 1. Norcamphor is a hexagonal, optically negative organic compound that melts at temperatures of 92–96°C. When deformed at temperatures in the experiments reported here, norcamphor develops microfabrics strongly resembling those of polycrystalline quartz under greenschist to amphibolite facies conditions. The reader is referred to Bons (1993) for a characterization of norcamphor's rheology as well as to Herwegh and Handy (1996) and Herwegh *et al*. (1997) for a discussion of the deformational behavior of norcamphor and a description of sample preparation techniques.

Strain localization patterns within the deforming sample were detected and quantified with the aid of very fine grains ($< 10\ \mu$m) of corundum which were mixed into the sample during preparation and behaved as passive strain markers during the experiment (Fig. 1b, method of Jessell, 1986). These particles were then used to calculate strain grids for the sample. The actual strain analysis comprised three steps, as shown schematically in Fig. 1(b): (1) Digitization of the marker particles' positions at different strains with the NIH IMAGE 1.57 (Rasband, 1997) macroroutine POINT DIGITIZER (Park, 1994); the location of the marker particles was digitized at shear strain intervals of between 0.15 and 0.25; (2) calculation of deformation grids and contouring of the axial ratios of the incremental strain ellipse (R_i values) for each node of the strain grid with the computer program MARKER ANALYSIS (Bons, 1993; Bons *et al*., 1993); strain grids were calculated at shear strain intervals of between 1 and 1.33; and (3) manual line drawings of high strain zones based on the R_i contours. To ensure that we did not mistake artefacts associated with contouring for strain heterogeneities, only R_i contour variations defined by several, consecutive cells of the strain grid were attributed to microshearing. In this way, we were able to map out continuous zones of high strain.

The resolution of strain in space and time within the sample depends on the number of marker particles per sample area, the average grain size of the norcamphor sample, the degree of localization (i.e. the strain intensity) and the number of digitized images recorded during the experiment. The spatial resolution of strain is better for smaller sizes of the calculated cells making up the strain grid. However, the density of marker particles places a lower limit on the cell size because at

Table 1. Experimental conditions

	HT–LS	HT–HS	IT–HS		LT–HS
T(°C)	25	25	10	10	4
T_h	0.81	0.81	0.77	0.77	0.76
shear strain rate	4.0×10^{-5}	5.5×10^{-4}	4.8×10^{-4}	5.5×10^{-4}	5.5×10^{-4}
max. shear strain (γ) attained	7.9	10.5	7.6	9	5
experimental duration (h)	55	5 1/4	4 1/2	4 1/2	2 1/2
calculations of strain increments	SPO, texture, strain $\gamma = 1.25$ (this work)	SPO, texture, strain $\gamma = 1$ Herwegh and Handy (1996)	SPO, strain $\gamma = 1.33$ (this work)	texture —	SPO, texture, strain $\gamma = 1$ (this work)

Table 2. Resolution of calculated strain grids

experiment	total number of digitized marker particles	number of marker particles per strain increment	number of calculated cells per strain increment	number of marker particles per calculated cell	number of marker particles per mm^2
HT–LS	1680	850	650	1.3	20
IT–HS	2150	1540	1040	1.5	44
LT–HS	1522	1150	600	1.9	23

least four marker particles are required to calculate one node of the strain grid (Bons *et al.*, 1993). In other words, at least one marker particle must be located within each cell of the calculated deformation grid to define accurately the positions of the four edges of one cell. Table 2 lists the particle densities used in our experiments and shows that the number of marker particles per calculated deformation cell ranges from 1.3 to 1.9. Our chosen grid size is therefore rather close at the limit of resolution. We return to this point below when discussing the mapping of intergranular microshears that accommodated small amounts of strain. For shear strains up to at least $\gamma = 8$, the method described above allowed us to resolve strain localization patterns from the sample scale down to the intergranular scale (microshears with a length of approximately 150–200 μm). We were only able to calculate incremental strain grids because at shear strains of $\gamma > 4$ the movement of corundum marker particles into and out of opposite sides of the field of view precluded a calculation of the finite strain grid for the entire sample.

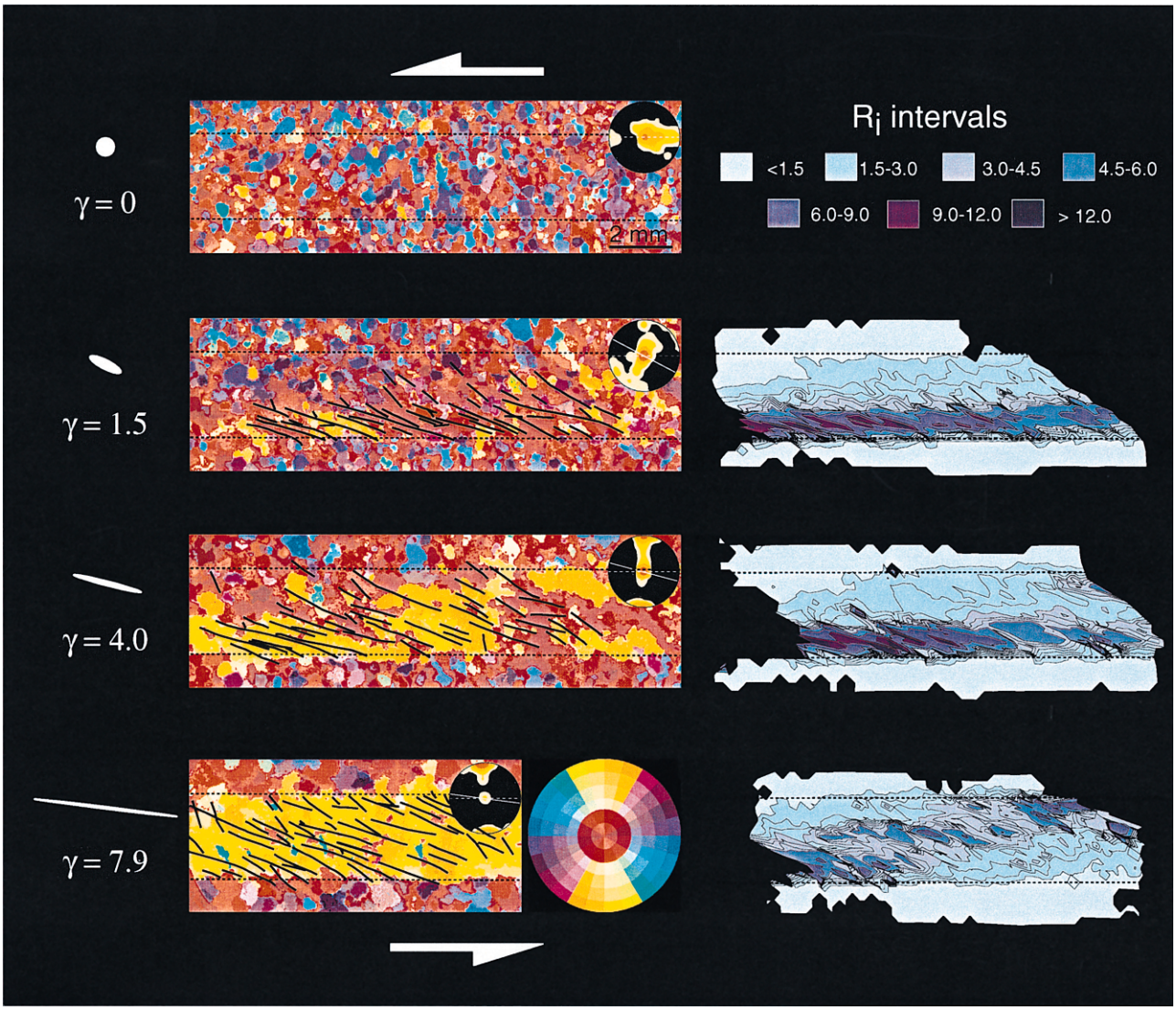

Fig. 2. Strain localization and microfabric evolution in the HT–LS experiment. Left column: Finite strain ellipses for the sample, colored *c*-axis orientation images containing black lines parallel to high strain zones, *c*-axis pole diagrams in corners of orientation images. Colors in the *c*-axis orientation images are keyed to the orientations shown in the pole diagram in the lower right corner of the left column. Contour intervals of the pole figures are 0.25, 1, 4, 16 times uniform distribution; Right column: sample images with contoured R_i values (axial ratios) of the incremental strain ellipses calculated for the following shear strain intervals: 0.25–1.5, 2.75–4.0, and 6.65–7.9. Dashed lines indicate sample shear zone boundaries.

Regarding the temporal resolution of strain, we found that the shear strain interval of 1–1.33 separating the calculated strain grids represents an acceptable compromise between two competing requirements: First, the interval must be sufficiently large for marker displacements to exceed the 10–20 μm width of the measuring field containing the digitization point (Fig. 1c). Second, the chosen strain interval should be small enough to monitor minor changes in strain heterogeneities. Our chosen interval guaranteed that most marker displacements were significantly greater than the aforementioned width of the measuring field. Displacements less than 10–20 μm could not be resolved. A drawback of the shear strain interval we chose was that it was too large to allow us to visualize the nucleation and early evolution of microshear zones. To compensate for this shortcoming, we inferred incipient strain localization patterns directly from videos and sequential photographs of the evolving microstructure. This was used to resolve microshears that accommodated small amounts of strain (S_b and S_c microshears described below).

The microfabric evolution was documented with computer integrated polarization microscopy (CIP: Panozzo Heilbronner and Pauli, 1993, 1994). The application of the CIP method to norcamphor experiments has already been described in Herwegh *et al.* (1997). This method allowed us to generate orientation images in which the *c*-axis orientations of individual grains in the aggregate are assigned characteristic colors (left columns in Figs 2–4). The *c*-axis positions corresponding to these colors are shown in the color-coded pole diagram of these figures.

Grain/domain particle and surface evolution were analyzed with the computer programs PAROR (Panozzo, 1983) and SURFOR (Panozzo, 1984), respectively. The reader is referred to Herwegh and Handy (1996) for a more detailed description of the analytical procedure. However, a resolution of grain boundaries based on color differences is limited at high

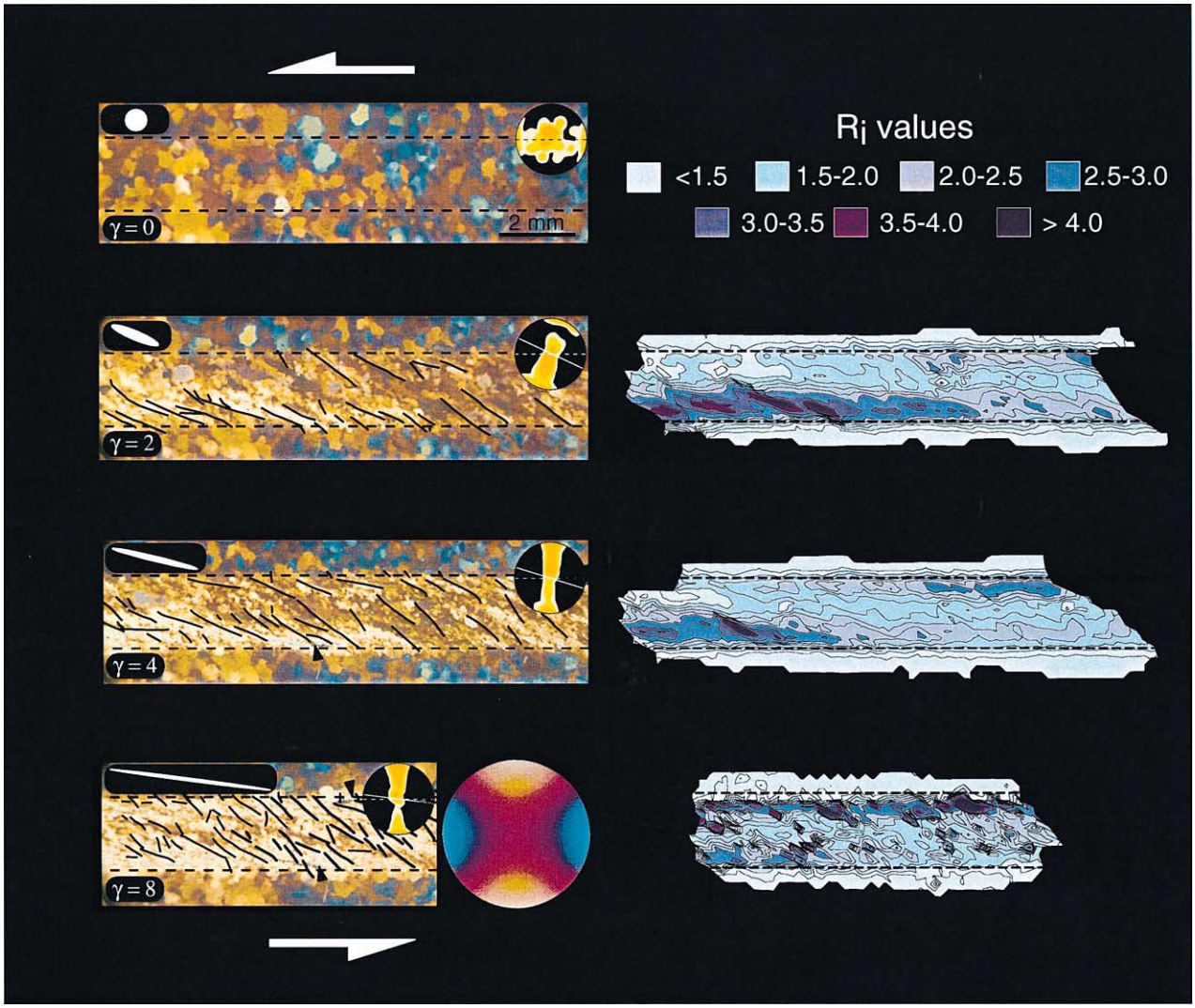

Fig. 3. Strain localization and microfabric evolution in the IT–HS experiment. Orientation images and sample images with contoured incremental strain as in Fig. 2. See Table 1 for shear strain interval used in calculating the incremental strain images.

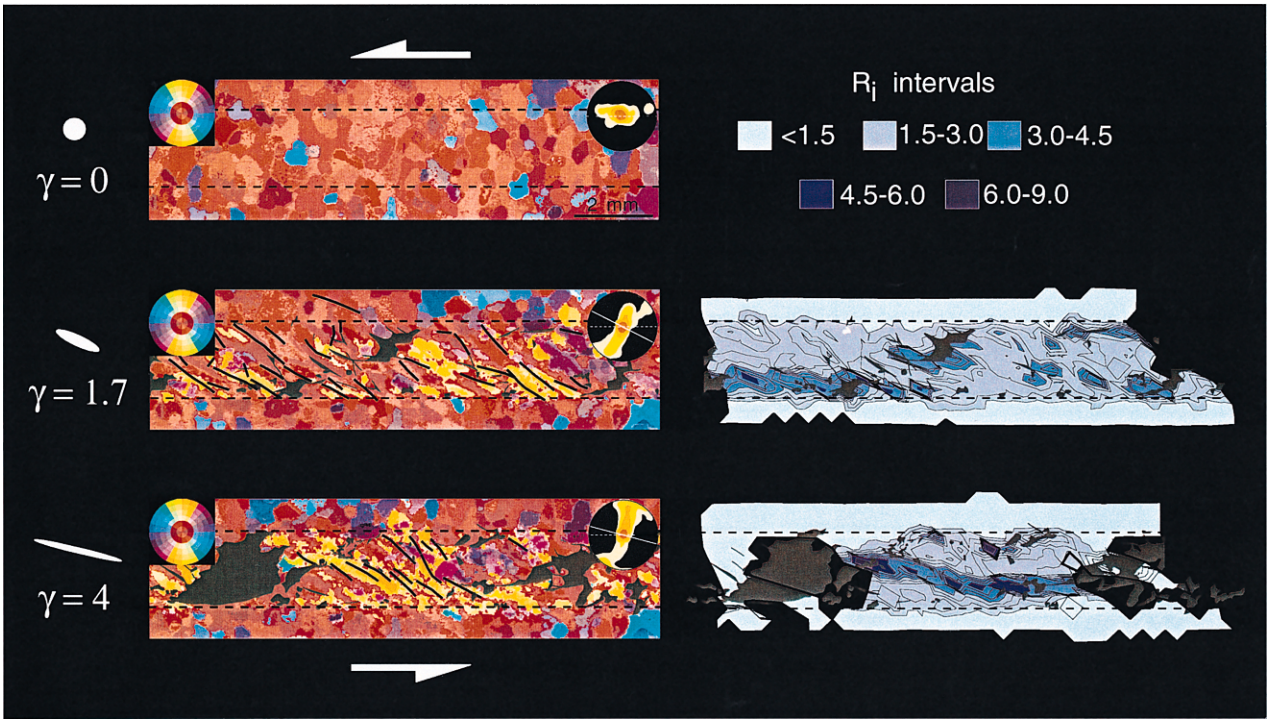

Fig. 4. Strain localization and microfabric evolution in the LT–HS experiment. Orientation images and sample images with contoured incremental strain as in Figs 2 and 3. See Table 1 for shear strain interval used in calculating the incremental strain images.

shear strains by the fact that most grains have similar crystallographic orientations. This restricted the analyses of the shape preferred orientation (SPO) to shear strains of 6 or less.

TEXTURAL AND MICROSTRUCTURAL EVOLUTION

Although a texture already exists at the beginning of the experiments (see detailed description in Herwegh *et al*., 1997), progressive strain is associated with the development of a pronounced CPO and the evolution of two different types of SPO in all experiments, as observed in the *c*-axis orientation images in Figs 2–4. The norcamphor *c*-axis patterns typically evolve from a cross-girdle to a stable, steady state texture (inset pole figures in the left column of Figs 2–4). The opening angle of the *c*-axis cross girdles varies as a function of strain rate and temperature, however, and the steady state texture either comprises two *c*-axis point maxima (HT–LS and HT–HS experiments) or a stable *c*-axis single girdle (IT–HS experiment). Also, the mechanisms involved in this textural evolution are closely related to the applied experimental conditions (see Herwegh *et al*., 1997). A glance at the *c*-axis orientation images in the left-hand columns of Figs 2–4 indicates that texture development is inhomogeneous, with the strongest CPO appearing first in the most highly strained parts of the sample (e.g. see yellow domains in Figs 2–4).

A grain SPO defined by the long axes of dynamically recrystallized grains develops at high angles to the SZB already during the first increments of strain (Figs 2–4). With progressive strain, groups of dynamically recrystallized grains with a similar crystallographic orientation coalesce to form domains whose long axes define a domain SPO at lower angles to the SZB. The angle of the grain and domain SPOs varies with the experimental conditions. The peaks in the particle and surface orientation diagrams for the HT–LS and IT–HS experiments (Table 3) indicate angles of the grain and domain SPOs, respectively, of 50–61° and 10–20° with respect to the SZB. In the LT–HS runs, however, the grain and domain SPOs form angles of about 37–43° and 22–29° to the SZB (Table 3). A glance at the *c*-axis orientation images (Figs 2–4) reveals that the domain SPO is more pronounced than the grain SPO. Thus, grains appear to be ephemeral features compared to domains. As shown in the next section, the relative intensity of the domain and grain SPOs as well as the varied SPO angles reflect the changing activity and rotation rates of intergranular microshears during deformation.

Interestingly, the width of the domains at shear strains of 2 and greater correlates directly with temperature and inversely with the strain rate, as shown in Fig. 5. The variable width of the domains reflects the dominant mechanism of dynamic recrystallization and hence also the resulting grain size; the relatively large domain widths in the high temperature experiments (HT–LS, HT–HS) correlates with the large grain size

Table 3. Particle (PAROR) and surface (SURFOR) orientations of grains and domains, (b/a): axial ratio short/long axis, α: angle between SZB and long axis (measured clockwise)

		Grains				Domains			
		PAROR		SURFOR		PAROR		SURFOR	
Experiment	γ	b/a	α	b/a	α	b/a	α	b/a	α
HT–LS	1.7	0.75	57	0.8	50	0.4	15	0.68	8
	4	0.79	57	0.81	58	0.45	10	0.77	15
	5.5	0.82	57	0.86	61	0.51	21	0.78	14
IT–HS	1.7	0.64	61	0.66	61	0.43	23	0.68	27
	3.5	0.67	56	0.69	57	0.37	17	0.46	20
	5.1	0.66	54	0.67	51	0.34	19	0.6	22
	7.7	0.71	55	0.73	55	0.35	17	0.47	17
LT–HS	1.7	0.69	37	0.78	38	0.4	28	0.56	29
	4	0.73	43	0.75	42	0.42	22	0.63	24

associated with a predominance of grain boundary migration recrystallization, whereas the narrower spacing in the intermediate and low temperature runs (IT–HS, LT–HS) relates to the fine grain size resulting from the high activity of subgrain rotation recrystallization. These and other associated grain-scale mechanisms in the norcamphor samples have already been documented in Herwegh and Handy (1996) and Herwegh *et al.* (1997).

STRAIN LOCALIZATION

The norcamphor experiments showed that strain localizes on both the sample and intergranular scales at all temperature and strain rate conditions. The localization patterns that evolve on these two scales are depicted in Figs 2–4, with intergranular microshears indicated by black lines superposed on the CIP images in the left columns, and with sample-scale shear zones imaged by the R_i contour maps of the sample in the right columns. A shear zone on the sample scale appears first at the lower left-hand corner of the field of view, then another appears at the upper right-hand corner. The occurrence of two sample-scale shear zones at diagonally opposite ends of the field of view reflects the localization of strain at the converging junctions of the frosted grips with the sample, as shown schematically in Fig. 6(a). Both the sequence of appearance of these shear zones as well as their length within the field of view in Figs 2–4 merely reflect the location of the field of view closer to the left-hand end of the experimental shear zone (dashed box in Fig. 6a). Thus, the experimental configuration governs the strain localization pattern, at least on the sample scale.

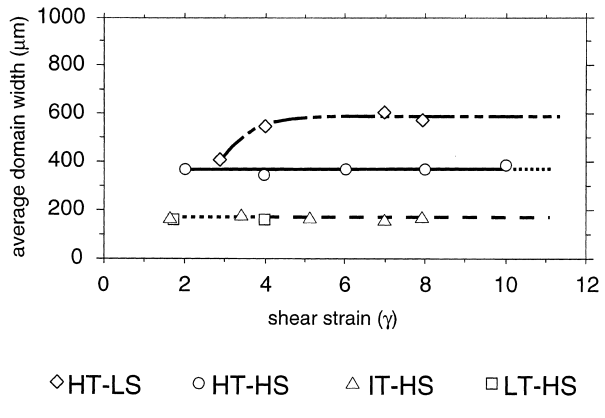

Fig. 5. Average domain width vs finite shear strain.

The shear strain profiles in Fig. 6(b) show that the sample-scale localization pattern varies with temperature and strain rate. In the HT–LS and LT–HS experiments, strain ultimately localizes in the middle of the sample, whereas most grain in the IT–HS run accrues adjacent to the sample boundaries (also, bottom row of Fig. 3). In the LT–HS experiment, crystal plasticity and dynamic recrystallization are not able to maintain strain compatibility on the sample scale. This results in fracturing and the opening of two big veins that transect the sample shear zone (see Fig. 4 and also fig. 9 in Herwegh *et al.*, 1997).

Grain-scale microshears are observed in all of the experiments and the long axes of these microshears form angles ranging from 90° to 10° or even less with respect to the SZB. The steepest microshears (70–90°) are not discernible on the strain contour maps because in this orientation they accommodate too little noncoaxial shear strain to be distinguishable from intracrystalline deformation. We therefore used photographic sequences like that in Fig. 7 to detect such low strain microshears. Note in this figure how a large grain is progressively dissected by vertically oriented discontinuities that separate domains of slightly different crystallographic orientation. With increasing shear strain these discontinuities rotate synthetically into parallelism with the SZB. We interpret these discontinuities to be initial deformation bands along which subgrain rotation recrystallization forms small new grains. Thus relative shear movements between the former host grain compartments seem to be accommodated implying that the deformation bands transform to Sb microshears.

Those shear zones oriented at angles less than 70° are imaged with black lines in the c-axis orientation images in Figs 2–4. Note that because the black lines

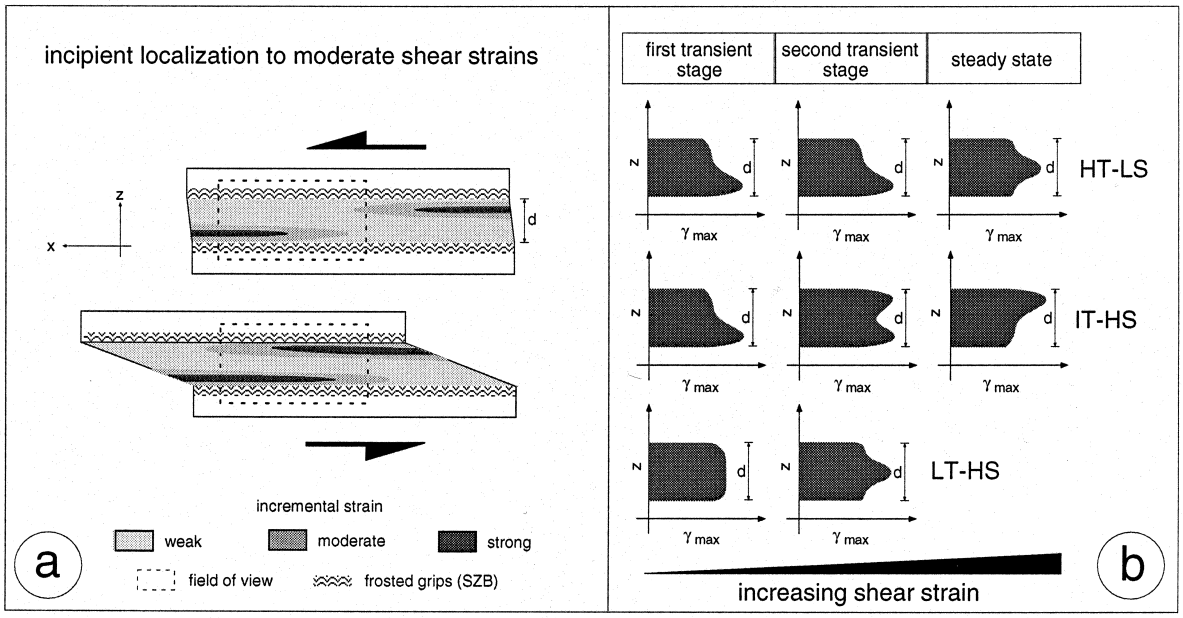

Fig. 6. Strain localization patterns on the sample scale: (a) Strain localization at diagonally opposite ends of the sample, dashed line indicates field of view. (b) Qualitative incremental shear strain profiles across the three types of experimental shear zones (see text for explanation).

in these figures are derived from the R_i contour maps, they outline only those shear zones which are most active, i.e. those which have accommodated the greatest amount of incremental strain. Two active microshear orientations are visible: One at low, 10–30° angles to the SZB and the other at relatively high, 30–70° angles to the SZB. These low- and high-angle orientations are henceforth termed S_a and S_b, respectively, following our earlier convention for microshears (Herwegh and Handy, 1996). We have also shown that the sense of shear along these microshears changes from predominantly antithetic parallel to S_b orientations, to predominantly synthetic parallel to S_a orientations as all microshears rotate toward parallelism with the SZB (fig. 7 in Herwegh and Handy, 1996). A third orientation, S_c identified in Herwegh and Handy (1996) at very low angles to the SZB (i.e. at $\alpha > 135°$) was also discerned locally in the HT–LS and IT–HS experiments (Figs 2 & 3). S_c-oriented microshears were only recognized with difficulty on the R_i contour maps, presumably because of the minor amount of incremental strain accommodated within them. However, the coincidence of R_i contour anomalies with strained grain boundaries (i.e. asymmetric grain boundary bulges, e.g. fig. 11 in Herwegh and Handy, 1996) parallel to the S_c orientation suggests that such microshears are indeed prevalent in our samples. These microshears are also manifest as small peaks in the grain SPO calculations of Table 3 at α angles of 135–180°.

The continuous nucleation and rotation of the microshears described above is best seen in Figs 8 and 9, where the rotation history of individual microshears is tracked during shear strain increments of 1.25 in the finite shear strain range of $\gamma = 3$–5. Figure 9(a) and (b) shows that the rotation rate is highest for active microshears with the S_b orientation (i.e. at high angles to the SZB), but decreases with decreasing angle between the microshears and the SZB. The concave shape of the curves in Fig. 9(a) indicates a nonlinear relationship between the microshear rotation rate and the angle between microshears and the SZB. In other words, the rotation rate of the microshears decreases as they approach parallelism with the SZB during progressive simple shear. This is depicted schematically in Fig. 9(c) for several generations of hypothetical microshears. Not surprisingly, the density of microshears as well as the strain accommodated within the microshears is greatest in the most highly strained parts of the samples (dark blue regions in R_i contour maps, Figs 2–4).

RELATIONSHIP OF MICROSTRUCTURE TO STRAIN LOCALIZATION

A conspicuous feature of the grain and domain SPOs in our samples is that they maintain a stable orientation with respect to the SZB throughout deformation. This is depicted in Fig. 10, where one can see that the α angle and axial ratios (b/a) of grains and domains remain constant with shear strain but deviate increasingly from the values calculated for the finite strain ellipse (dashed lines in Fig. 10, calculated after formulas 1 and 2 derived in Ramsay and Graham, 1970 and Ramsay, 1967, respectively). It is interesting to note that grains attain a stable SPO already at shear strains less than 1.5, whereas the long axes of

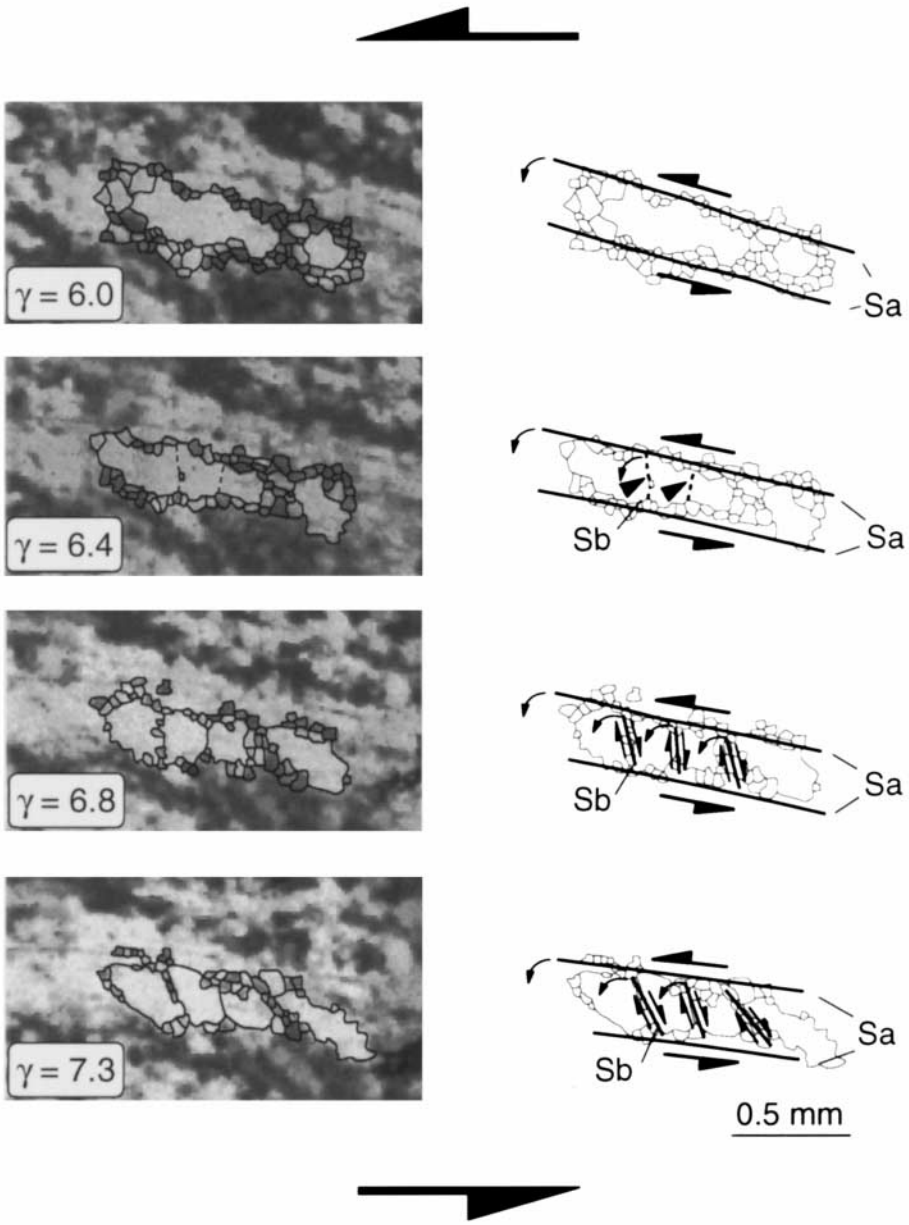

Fig. 7. Relationship of microscale strain localization to microstructure in the IT–HS experiment. Nucleation and growth of new S_b microshears between rotated S_a microshears at intermediate to high finite shear strains. Note that microshears coincide with grain and domain boundaries marked by dynamic recrystallization. See text for further explanation.

the domains first follow the predicted rotation path of the finite strain ellipse and only become stable at shear strains above 3.5.

We attribute this discrepancy between observed and theoretical α and b/a values of the SPOs to intergranular microshearing, as described in the previous section. Microshears seem to nucleate already at the onset of deformation along grain boundaries that form a high angle with the SZB. With increasing shear strain, these microshears undergo progressive synthetic rotation towards the SZB until they attain a low angle with respect to the SZB, characteristic of the S_a orientation. High-angle microshears continue to nucleate along steeply oriented microstructural anisotropies (e.g. grain and kinkband boundaries). At yet higher shear strains, these high-angle microshears transect low angle domains that are bounded by rotating microshears with the S_a orientation (Fig. 7).

The significance of the S_b and S_a microshear orientations is that they correspond, respectively, with the grain and domain SPOs described above. Thus, the coexistence of two differently oriented SPOs reflects two aspects of intergranular strain localization: (1) the nucleation of high-angle microshears that accommodate increasing amounts of shear strain as they acquire an S_b orientation, and (2) the initial decrease and subsequent increase in the amount of strain accommodated as the microshears rotate out of the S_b into the S_a orientation. If the amount of strain

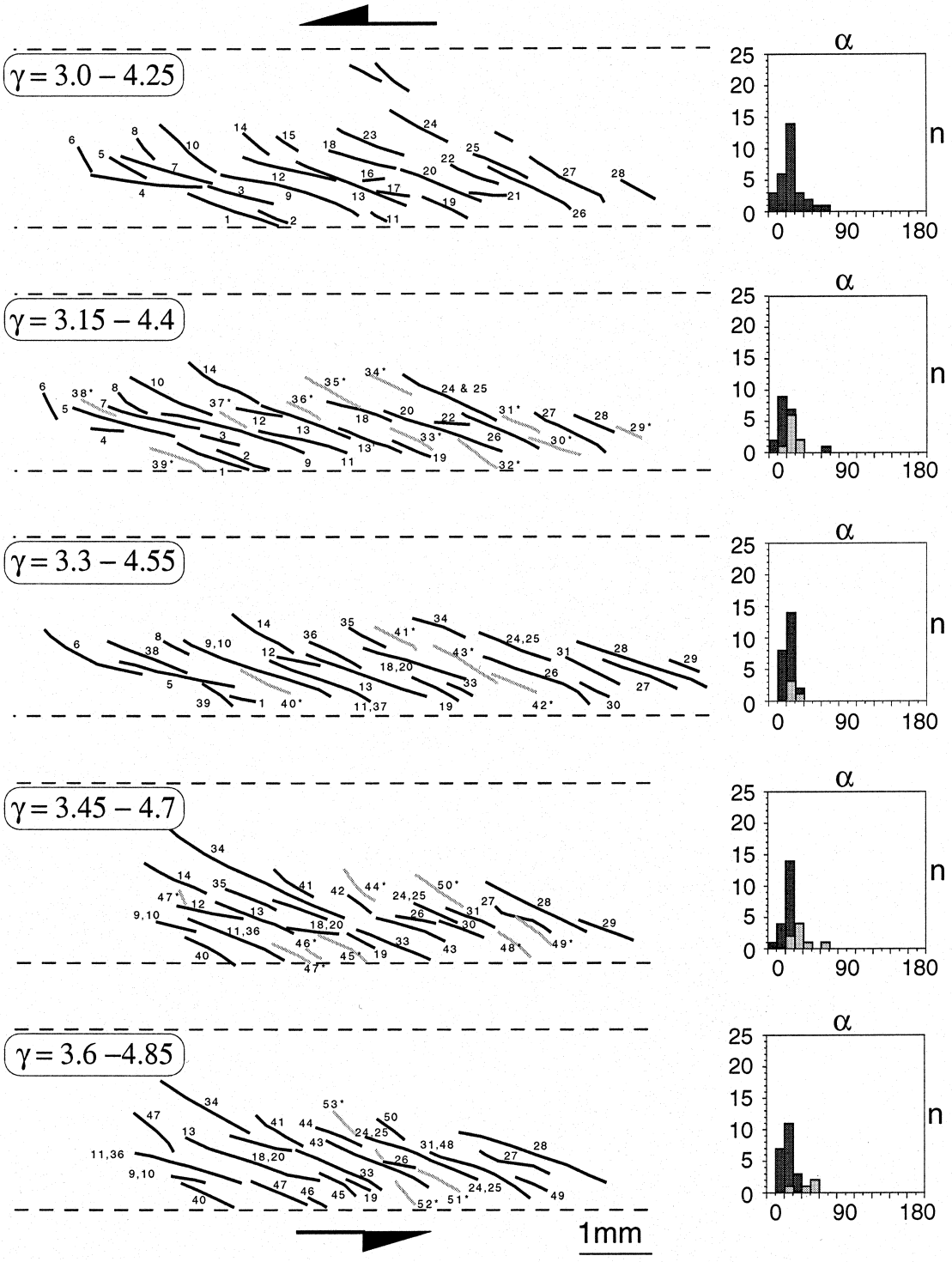

Fig. 8. Maps of numbered microshear zones during different increments of progressive shear strain in the HT–LS experiment. Black lines: older S_b microshears rotating into orientations typical of those for S_a microshears. Grey lines: younger S_b microshears. Dashed lines: shear zone boundaries (SZB). Histograms show number of microshear zones, n at an angle α to the SZB.

accommodated by the microshears did not vary with orientation, then we would expect the SPO distribution to be continuous rather than bimodal. The fact that it is bimodal, however, and that the domain SPO is more pronounced than the grain SPO (recall Figs 2–4) reflect the lower rotation rate and greater activity of S_a-oriented microshears, as described in the previous section.

Interestingly, the α angle and b/a ratio of grain and domain SPOs is generally independent of shear strain in all samples in which dynamic recrystallization is the predominant mechanism (HT–LS, HT–HS and IT–HS

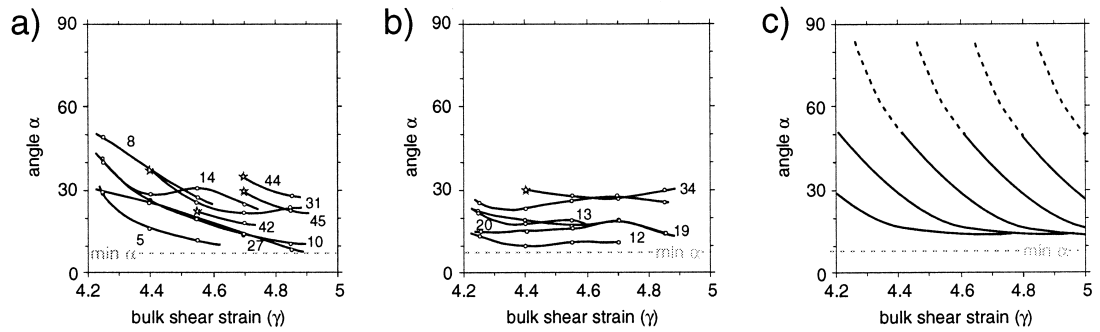

Fig. 9. Rotation of microshear zones reflected in plots of the angle between microshear zones and SZB, α, vs finite shear strain for the finite shear strain interval from 4.2 to 5.0. Numbers correspond to numbered microshears in Fig. 8: (a) Curves for microshears with initially high values of α; (b) Curves for microshears with low values of α; (c) Hypothetical curves synthesized from curves in (a) and (b) depicting changing rotation rates of individual microshears. Note that the steeper the curve, the higher the rotation rate of the microshear.

experiments), irrespective of temperature and strain rate (Fig. 10). This suggests that the microstructure primarily reflects the strain configuration rather than the externally imposed physical conditions (i.e. temperature and strain rate) of deformation. Temperature and strain rate do affect the spacing between the microshears, however, as indicated by the observation above that grain size and domain width (i.e. the spacing between S_b- and S_a-oriented microshears, respectively) vary with the mechanism of dynamic recrystallization (subgrain rotation vs grain boundary migration, recall Fig. 5). Thus, the α and b/a parameters appear to be good indicators of the overall strain configuration, whereas the grain size and domain width reflect the temperature and strain rate conditions.

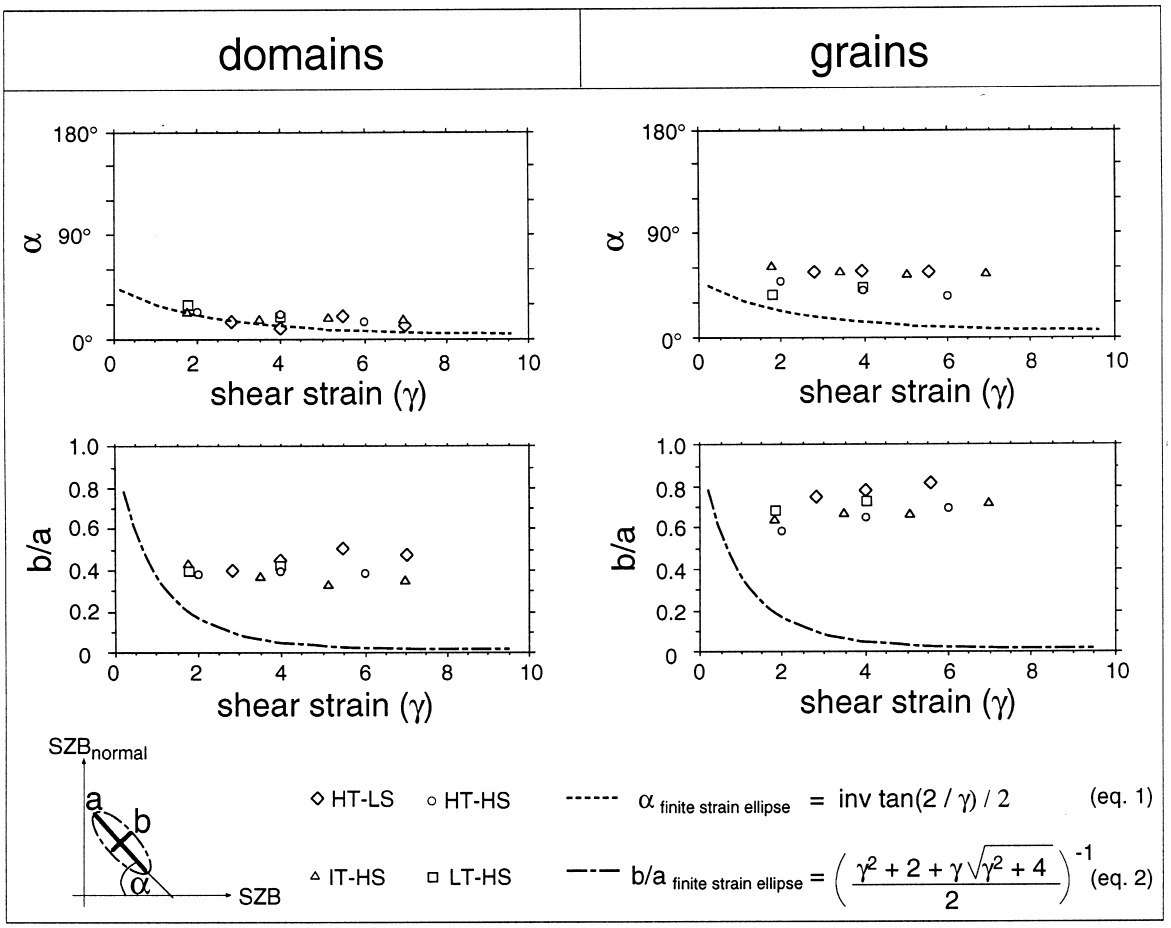

Fig. 10. Change in orientation and axial ratios of grains and domains with progressive simple shear. Values of α, a, and b derived from Table 3. Formulae for $\alpha_{\text{finite strain ellipse}}$ [equation (1)] and $b/a_{\text{finite strain ellipse}}$ [equation (2)] taken from Ramsay and Graham (1970) and Ramsay (1967), respectively.

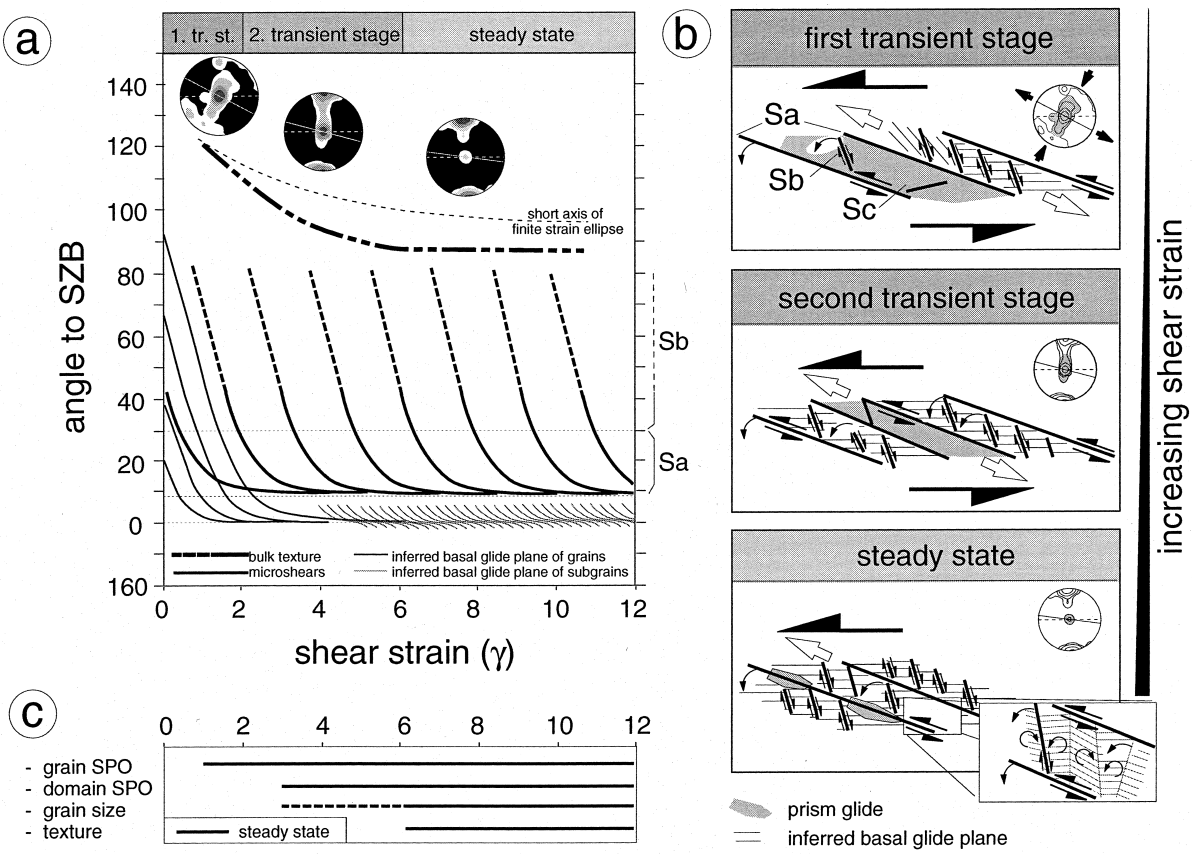

Fig. 11. Summary of strain localization on different scales and of microfabric evolution. (a) Changing rotation rates of strain heterogeneities and relationship of these heterogeneities to texture evolution; (b) Nucleation and growth of microshears and relationship to intracrystalline glide with progressive shear strain; (c) Shear strains at onset of steady state in different microfabric elements (see text for explanation).

Garcia Celma (1982) and Pauli *et al.* (1996) describe mylonitic quartz microfabrics consisting of domains with two oppositely oriented oblique SPOs. The lack of such SPOs in our experiments indirectly supports Garcia Celma's interpretation that pure or at least general shear are required to generate such microfabrics.

A NEW MODEL FOR THE ORIGIN AND EVOLUTION OF DOMAINAL AND GRAIN SHAPE PREFERRED ORIENTATIONS AND SOME GEOLOGICAL IMPLICATIONS

Our experiments indicate that microfabric development in mylonite is intimately linked to strain localization on both the inter- and intragranular scales. The hypothetical model in Fig. 11 shows how both microshears (thick lines in Fig. 11a) and crystal slip systems (thin lines in Fig. 11a) rotate after their nucleation, respectively, along grain boundaries and within newly crystallized grains. As these anisotropies rotate into (and in rare cases, even out of) parallelism with the sample SZB (see behavior of subgrains in Fig. 11a & b), local strain compatibility within the sample is no longer maintained, leading to renewed microshear nucleation and dynamic recrystallization. This process is inferred to be cyclic on both the granular and supergranular scales. The rotation of the crystal slip systems is reflected in the CPO, whereas the rotation and relative activity of the microshears is manifest in the grain and domain SPOs. In norcamphor, these microfabric features attain steady state at different shear strains. For example, grain SPO becomes strain invariant already at $\gamma = 1.5$, domain SPO at $\gamma = 3$, and CPO at $\gamma = 6$. The strain at which dynamically recrystallized grain size becomes independent of strain varies with the dynamic recrystallization mechanism and therefore also with the temperature and strain rate of deformation: steady state grain size is generally attained at lower strains for subgrain rotation than for grain boundary migration recrystallization (Herwegh *et al.*, 1997). This is consistent with the general observation that CPO survives late changes in the kinetic boundary conditions, whereas grain size and grain SPO are prone to late-stage resetting (e.g. Simpson, 1980 and references therein).

Our experiments on norcamphor have shown that grain SPO in mylonite forms early rather than late during progressive noncoaxial shear, as already proposed by Lister and Snoke (1984). The angle of the grain and domain SPOs in dynamically recrystallized

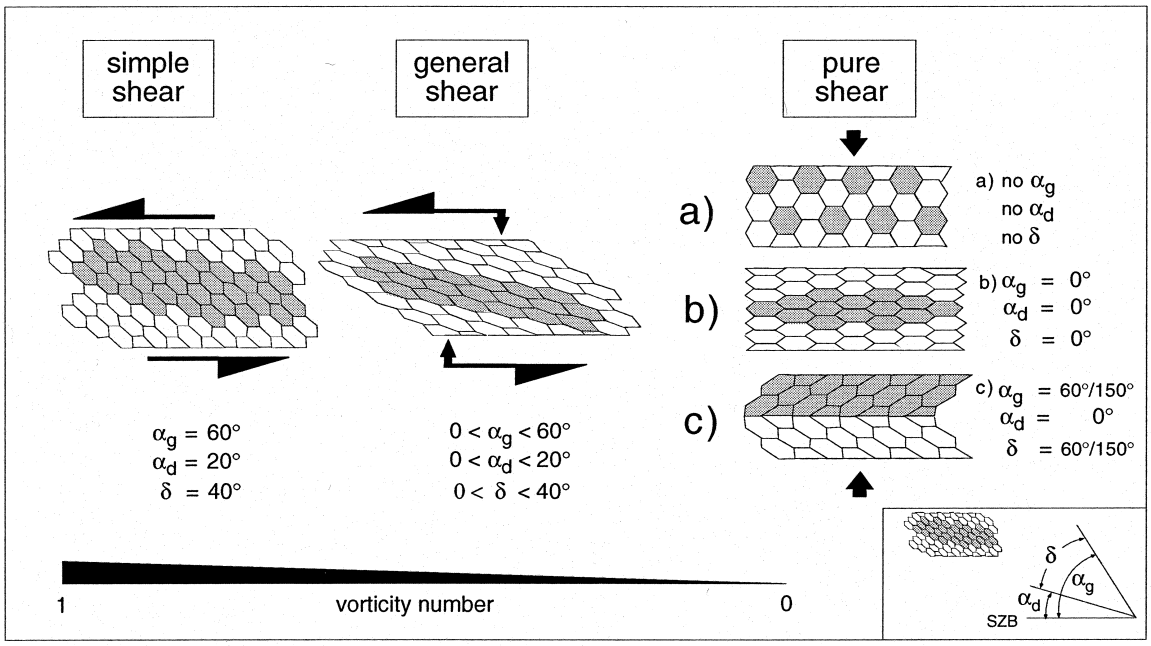

Fig. 12. Changes in steady state SPOs in dependence of the principal stress direction during plane strain deformation (see text for explanation).

aggregates reflect the bulk strain configuration: In our simple shear experiments for example, the grain and domain SPOs are oblique both with respect to each other ($\delta' = 40°$) and to the shear zone boundary ($\alpha = 60°$ for dynamically recrystallized grains, $\alpha = 20°$ for domains). Similar relationships are ubiquitous in natural, noncoaxially deformed mylonites and might be also active in aggregates that were experimentally deformed in simple shear (calcite: fig. 8e and f in Schmid *et al.*, 1987; quartzite: fig. 7 in Dell'Angelo and Tullis, 1989). In contrast, experimental uniaxial shortening of quartzite involving dynamic recrystallization yielded grain and domain SPOs that are parallel to the SZB (figs 5 and 6 in Tullis *et al.*, 1973). We therefore infer that the angle, δ, between the grain and domain SPOs is related both to the degree of noncoaxiality and to the shape of the strain ellipsoid for the increments of strain accrued just prior to the end of deformation.

The model in Fig. 12 depicts an idealized set of SPO patterns for transitions from bulk pure shear to bulk simple shear, plane strain mylonitization of quartz. In this model, the angle δ between grain and domain SPOs varies from 0° for pure shear (case b in Fig. 12) to about 40° for simple shear. Shear configurations between these two end-members are expected to yield δ values between 0 and 40°, with values nearer to 40° corresponding to vorticity numbers approaching 1. One limitation of this relationship, however, is that aggregates subjected to a large component of coaxial shear at temperatures and strain rates favoring grain boundary migration recrystallization often have equigranular grain shapes and lack domain SPOs (e.g. a in Fig. 12 and fig. 4b in Handy *et al.*, 1996). In this case, a δ value cannot be defined. Pure shear microfabrics in which subgrain rotation recrystallization predominated often show similar δ values as found in simple or general shear, but fortunately can be distinguished from the latter by the fact that two grain SPOs (rather than just one) are developed. These SPOs are symmetrically disposed with respect to the main foliation. Presumably, the development of such grain SPOs is related to the partitioning of strain along conjugate sets of microshears (e.g. c in Fig. 12 and Garcia Celma, 1982; Pauli *et al.*, 1996).

Our model is obviously tentative in the absence of experimental and theoretical studies on the effects of strain configuration and vorticity on the orientation of intergranular microshears, textures and microstructures. Nevertheless, we believe that the angle δ between grain and domain SPOs in monomineralic mylonite bears potential for providing at least qualitative estimates of the vorticity number, even when other microfabric elements such as grain size and texture are not at steady state. Analogue experiments in which kinematic vorticity is varied should allow one to test this model.

Acknowledgements—We thank Guido Schreurs for his comments on an earlier version of this manuscript and the two journal referees, Mark Jessell and Janos Urai, for their constructive reviews. The financial support of the Swiss National Science Foundation (Profil-2 grant 21-30598.91, project grant 21-33814.92) is acknowledged with gratitude.

REFERENCES

Bons, P. D. (1993) Experimental deformation of polyphase rock analogues. *Geologica Ultrajectina* **110,** 207 pp.

Bons, P., Jessell, M. W. and Passchier, C. W. (1993) The analysis of progressive deformation in rock analogue. *Journal of Structural Geology* **15,** 403–412.

Brunel, M. (1980) Quartz fabrics in shear zone mylonites: Evidence for a major imprint due to late strain increments. *Tectonophysics* **64,** T33–T44.

Burg, J. P., Wilson, C. J. L. and Mitchell, J. C. (1986) Dynamic recrystallization and fabric development during simple shear deformation of ice. *Journal of Structural Geology* **8,** 857–870.

Dell'Angelo, L. N. and Tullis, J. (1989) Fabric development in experimentally sheared quartzites. *Tectonophysics* **169,** 1–21.

Garcia Celma, A. (1982) Domainal and fabric heterogeneities in Cap de Creus quartz mylonites. *Journal of Structural Geology* **4,** 443–455.

Handy, M. R., Herwegh, M., Kamber, B., Teitz, R. and Villa, I. (1996) Geochronologic, petrologic and kinematic constraints on the evolution of the Err-Platta boundary, part of a fossil continent–ocean suture in the Alps (eastern Switzerland). *Schweizerische Mineralogische und Petrographische Mitteilungen* **76,** 453–474.

Herwegh, M. and Handy, M. R. (1996) The evolution of high temperature mylonitic microfabrics: evidence from simple shearing of a quartz analogue (norcamphor). *Journal of Structural Geology* **18,** 689–710.

Herwegh, M., Handy, M. and Panozzo Heilbronner, R. (1997) Temperature and strain rate dependent microfabric evolution in monomineralic mylonite: evidence from *in-situ* deformation of norcamphor. *Tectonophysics* **280,** 83–106.

Jessell, M. W. (1986) Grain boundary migration and fabric development in experimentally deformed octachloropropane. *Journal of Structural Geology* **8,** 527–542.

Karato, S. and Masuda, T. (1989) Anisotropic grain growth in quartz aggregates under stress and its implication for foliation development. *Geology* **17,** 695–698.

Knipe, R. J. and Law, R. D. (1987) The influence of crystallographic orientation and grain boundary migration on microstructural and textural evolution in an *S–C* mylonite. *Tectonophysics* **135,** 155–169.

Lister, G. S. and Snoke, A. W. (1984) *S–C* mylonite. *Journal of Structural Geology* **6,** 617–638.

Lloyd, G. E., Law, R. D., Mainprice, D. and Wheeler, J. (1992) Microstructural and crystal fabric evolution during shear zone formation. *Journal of Structural Geology* **14,** 1079–1100.

Means, W. D. (1989) Synkinematic microscopy of transparent polycrystals. *Journal of Structural Geology* **11,** 163–174.

Panozzo Heilbronner, R. and Pauli, C. H. (1993) Integrated spatial and orientation analysis of quartz *c*-axis by computer-aided microscopy. *Journal of Structural Geology* **15,** 369–383.

Panozzo Heilbronner, R. and Pauli, C. (1994) Orientation and misorientation imaging: integration of microstructural and textural analysis. In *Textures of geological materials*, eds. H. J. Bunge, S. Siegesmund, W. Skrotzki and K. Weber, pp. 147–164. DGM Informationsgesellschaft.

Panozzo, R. (1983) Two-dimensional analysis of shape-fabric using projections of digitized lines in a plane. *Tectonophysics* **95,** 279–294.

Panozzo, R. (1984) Two-dimensional strain from the orientation of lines in a plane. *Journal of Structural Geology* **6,** 215–221.

Park, Y. (1994) Microstructural Evolution in Crystal-Melt Systems. Unpublished Ph.D. thesis of the State University of New York at Albany.

Pauli, C., Schmid, S. M. and Panozzo Heilbronner, R. (1996) Fabric domains in quartz mylonites: localized three dimensional analysis of microstructure and texture. *Journal of Structural Geology* **18,** 1183–1203.

Ramsay, J. G. (1967) *Folding and Fracturing of Rocks*. MacGraw-Hill, New York, p. 568.

Ramsay, J. G. and Graham, R. H. (1970) Strain variation in shear belts. *Canadian Journal of Earth Sciences* **7,** 786–813.

Rasband, W. (1997) *Image 1.61. National Institute of Health.* Research Services Branch NIMH.

Ree, J. H. (1991) An experimental steady-state foliation. *Journal of Structural Geology* **13,** 1001–1011.

Schmid, S. M., Panozzo, R. and Bauer, S. (1987) Simple shear experiments on calcite rocks: rheology and microfabric. *Journal of Structural Geology* **9,** 747–778.

Simpson, C. (1980) Ductile shear zones: A mechanism of rock deformation in the orthogneisses of the Maggia nappe, Ticino, Switzerland. Ph.D. thesis from the ETH Zürich.

Simpson, C. and Schmid, S. M. (1983) An evaluation of criteria to deduce the sense of movement in sheared rocks. *Bulletin of the Geological Society of America* **94,** 1281–1288.

Tullis, J., Christie, J. M. and Griggs, D. T. (1973) Microstructures and preferred orientations of experimentally deformed quartzites. *Bulletin of the Geological Society of America* **84,** 297–314.

Urai, J. L. (1987) Development of microstructure during deformation of carnallite and bischofite in transmitted light. *Tectonophysics* **125,** 251–263.

Zhang, S. and Karato, S. (1995) Lattice preferred orientation of olivine aggregates deformed in simple shear. *Nature* **375,** 774–777.